Experimental Thermal and Fluid Science 112 (2020) 110017

Contents lists available at ScienceDirect

Experimental Thermal and Fluid Science

journal homepage: www.elsevier.com/locate/etfs

Spectral emissivity and temperature of heated surfaces based on spectrometry and digital thermal imaging – Validation with thermocouple temperature measurements

Weijie Yan[a,b,**], Aidin Panahi[b], Yiannis A. Levendis[b,*]

[a] School of Electrical and Power Engineering, China University of Mining and Technology, No.1, Daxue Road, Xuzhou, Jiangsu 221116, China
[b] Mechanical and Industrial Engineering Department, Northeastern University, Boston, MA 02115, USA

ARTICLE INFO

Keywords:
Temperature measurement
Spectral emissivity
Spectrum analysis
Thermocouple

ABSTRACT

The spectral emissivity of an object is required to measure its temperature remotely, based on thermal imaging from a high-speed digital camera. However, it is often difficult to obtain the spectral emissivity of objects under transient conditions, as is the case with burning fuels; hence, the accuracy of the temperature measurement is compromised. This manuscript describes a method of temperature measurement of objects with simultaneous use of a spectrometer and a high-speed camera. The method was demonstrated by viewing the bead of an R-type thermocouple heated by a premixed natural gas flame to temperatures in the range of 1450–1530 K, and by comparing such remote temperature measurements with those obtained based on the thermocouple's voltage output. The spectral emissivity of the heated thermocouple was acquired from spectroscopic analysis of its output radiation, in the wavelength range of 500–1000 nm. It was shown that the thermocouple approached graybody behavior at the upper end of this band. It was also shown that spectral emissivity of R-type thermocouple is close to the emissivity of S-type thermocouple, reported in the literature in the wavelength range of 500–700 nm and, also, close to the emissivity of pure platinum. This suggests that the effect of rhodium on the platinum emissivity is negligible. The temperature of the R-type thermocouple was measured at four different flame conditions (by varying the fuel/air equivalence ratio) using the spectrometer and the high-speed camera, and it was compared with the thermocouple temperature measurements. The flame was either steady or unsteady; the latter condition was implemented to evaluate the transient response of the measurements. In both cases, the comparison showed that the results of the three different temperature measurement methods have very high consistency and were within 11 K in the explored temperature range. Hence, this method is suitable for temperature measurements of objects of varying temperature and emissivity, such as solid fuel particles during their combustion.

1. Introduction

Temperature is a parameter of outmost importance in combustion, affecting the efficiency of combustion and the generation of pollutants therefrom [1]. Hence, the accurate measurement of temperature is of great significance for improving the energy conversion efficiency of a fuel and for determining reaction mechanisms and rates [2–5]. Thermometry based on emitted radiation is a non-contact temperature measurement method, hence, it does not interfere with an object and its operation is simple and non-intrusive. As a result, this method finds a wide range of applications in temperature measurement of hot surfaces [6–9], solid fuel particles and particle-laden flames [10–20]. Image sensors or spectral sensors are typically used for collecting radiation from metal or refractory surfaces, burning solid fuels or burning soot particulates. Temperature is then calculated based on the functional relationship between radiation intensity, temperature and emissivity of the targeted object. However, as the emissivity of objects is often unknown a priori, assumptions need to be made; thus the accuracy of the temperature measurement is compromised. In this work, combined spectrometric and thermometric techniques were used to measure the spectral emissivity and the temperature of a heated thermocouple bead. The accuracy of the thermocouple temperature measurement using these techniques was assessed by comparison with temperature readings based on the thermoelectric voltage output of this device. The

* Corresponding author.
** Corresponding author.
E-mail addresses: yanweijie@cumt.edu.cn (W. Yan), y.levendis@northeastern.edu (Y.A. Levendis).

https://doi.org/10.1016/j.expthermflusci.2019.110017
Received 19 October 2019; Received in revised form 22 November 2019; Accepted 1 December 2019
Available online 03 December 2019
0894-1777/

Nomenclature

$\varepsilon(\lambda)$	the spectral emissivity
$\eta(\lambda)$	the spectral response efficiency function of the camera's i channel
λ_1	the lower wavelength limits of spectral response of high-speed camera
λ_2	the upper wavelength limits of spectral response of high-speed camera
T_c	the 2D temperature distribution of the measured object (K)
S	the output image intensity of the high-speed camera
E_i	the radiation intensity measured by high-speed camera (W/m^2 sr)
T_s	one-dimensional temperature measured by the spectrometer (K)
j	the number of measured effective wavelengths within of the spectrometer

Greek symbols

τ	the shutter time of the high-speed camera

purpose of this effort was to formulate a non-intrusive method for conducting future measurements on combined spectral emissivity and temperature of burning pulverized solid fuels.

Information on the two-dimensional (2D) radiation of an object can be obtained by using the image sensor of a digital camera; therefrom two-dimensional (2D) [21–23] or, even, three-dimensional (3D) temperature fields [24–26] can be reconstructed. However, image sensors can only detect radiation information at a limited wavelength range, corresponding to their red (R), green (G) and blue (B) channels. Hence, information on the object's emissivity at those wavelengths is necessary. Smart et al. [27] measured the temperature of an oxygen-rich combustion flame using a color camera and analyzed the results with the emissivity model of soot of Hottel and Broughton [28]. Kuhn et al. [29] measured the temperature of a silicon carbide (SiC) filament using an SLR camera to eventually obtain the temperature of an ethylene/air diffusion flame. The SiC filament was regarded as a graybody in the visible region, with a constant emissivity of 0.88 [30]. Vicariotto et al. [31] also used a method similar to that of Ref. [29] to obtain the 2D temperature distribution of a methane/air diffusion flame. Sun et al. [32] used a color camera to measure the temperature of a heavy oil flame; and calculated the flame emissivity using Hottel and Broughton's soot emissivity model. Draper et al. [33] used a broadband, RGB, two-color pyrometry technique to measure the 2D distribution of temperature and emissivity of a pulverized coal flame and reported a difference from the graybody model, in the temperature range of 2100–2660 K. Khatami and Levendis [34] used a three-wavelength pyrometer [35] to measure temperature profiles of single particles of pulverized coal, during their entire combustion histories. They assumed that the emissivity of pulverized coal char particles was either independent of wavelength (graybody) or a linear function of wavelength in the range of 650–1000 nm. They reported a temperature difference in the order of 40 K between these two assumptions. Deep et al. [36] used an SLR camera to measure the temperature distribution of the radiation shock layer; they assumed that the measured object behaved as a graybody in the wavelength range of 400–700 nm. It is evident from such studies, which were based on thermal radiation sensors, that the accuracy of temperature measurement depends on the assumptions made on the spectral emissivity of the object as a function of wavelength.

In contrast to image sensors, radiation information from an object at multiple wavelengths can be obtained based on spectral sensors. In this case, the temperature and spectral emissivity can be measured simultaneously, assuming a spectral emissivity model [37]. Khan et al. [38] used the least square method to simultaneously measure the temperature and emissivity of a platinum (Pt) strip, in the temperature range of 913–1255 K, based on the visible and near-infrared radiation spectrum. They reported a relative measurement error in temperature of less than 6%. They also reported calcualted Platinum strip emissivities to be in the range of 0.24–0.44, at wavelengths in the range of 400–1000 nm and temperatures in the range of 913–1255 K. Wen et al. [6,7] measured the temperature and emissivity of stainless steel and aluminum alloys using radiation spectra and discussed the effects of different emissivity model assumptions. The spectral emissivity of stainless steel at 700 K was expressed as a second-order polynomial in the band of 2000–4700 nm, and the average emissivity was ~0.2. The aluminum alloy behaved as graybody at 700 K with an emissivity of 0.1. Xing et al. [39] designed a multi-wavelength pyrometer using a micro spectrometer and developed a spectral emissivity model that is independent of wavelength but it is dependent on temperature. Their experiments were carried out on a blackbody heated to 1260–1310 K and viewed through filters in the band of 580–760 nm. The transmissivities of these filters were known, so these transmissions were treated as emissivity of a real body at the temperature of the black body. They reported that their absolute error of measurement was less than 12 K, and the relative error was less than 1%. Wang et al. [9] measured the spectral emissivity of stainless steel using a Fourier transform infrared spectrometer in conjunction with a polynomial emissivity model. Their results showed that the emissivity of stainless steel in the wavelength range of 2000–6000 nm increases from 0.357–0.456 to 0.439–0.491 with increasing temperature from 1073 to 1373 K (± 2.8 K). Sun et al. [40] used a portable fiber-optic spectrometer to measure the temperature and emissivity of a pulverized coal flame in a utility boiler. They found that the pulverized coal flame was gray in the band of 500–1000 nm, however the flame temperature and emissivity varied with the location in the combustion zone. They reported emissivities in the range of 0.1–0.4 and temperatures in the range of 1360–1460 K. It should be noted that this method was only suitable for measurement of temperature and emissivity of graybodies. Yan et al. [15] measured the temperature and emissivity of municipal solid waste incineration flames in the wavelength band of 500–900 nm, using a method similar to that of Ref. [40]. The flames were found to be gray in this band, their emissivities were in the range of 0.2–0.45, and their temperatures were in the range of 1000–1500 K. Nonetheless, there are characteristic spectral lines of Na (590 nm) and K (767 nm), which could cause interference to multi-spectral temperature measurements. Parameswaran et al. [41] measured the temperature and emissivity of a coal gasifier flame with a spectrometer. They reported that the flame was gray in the band of 650–710 nm, but the emissivity was related to temperature (in the range of 1200–2100 K) and varied from 0.1 to 0.7. In subsequent research [42], the same authors reported that in a coal gasification flame temperatures of petroleum coke measured by a spectroscopic method were higher than those measured by thermocouples. In summary, one-dimensional measurements of temperature and emissivity can be obtained simultaneously with spectral sensors. However, the accuracy of the measured results can be affected if the temperature and emissivity of the object are not spatially uniform.

Radiation from high temperature objects can also be detected by hyperspectral sensors with spatial and spectral resolutions. Thus, it has been possible to simultaneously measure the two-dimensional temperature distribution and the spectral emissivity distribution. Liu et al. [43] measured the temperature and emissivity of ethylene diffusion flames using hyperspectral images in the visible band and reported that the emissivity decreased at increasing wavelengths. Devesse et al. [44] used hyperspectral images to measure the temperature of stainless steel, at temperatures in the range of 1800–2000 K, and reported a

measurement relative error less than 10%. Fu et al. [45] measured the temperature of metal surfaces in a supersonic plasma jet environment using a high-speed hyperspectral camera; however, the temporal resolution was not sufficiently high for recording rapid changes of temperature. Si et al. [46] used a hyperspectral camera for simultaneous measurements of temperature and emissivity of single particles of pulverized coal. In their experiments, a stepper motor was used to enable the hyperspectral camera to follow the particle movement, since the camera used in the experiment required scanning imaging. Compared to spectrometer and color cameras, hyperspectral camera needs more time to process the large amounts of acquired data, so it is currently difficult to obtain hyperspectral images at high sampling rates.

The high-speed camera only collects radiation images at three channels: red, green and blue (R, G, B). Hence, by comparison with the hyperspectral camera, it has a much higher sampling frequency, high output image resolution, and lower cost. As a result, high-speed digital cameras have been widely used for temperature measurements of different transient objects [47–52] and for morphological change measurements of burning particles [53,54]. However, the radiation information conveyed by high-speed cameras is limited, and accurate temperature measurement also must depend on the knowledge of the spectral emissivity of the measured object. Hence, in this investigation a 2D temperature measurement method was implemented, combining the advantages of spectrometers and high-speed cameras. The method was validated with experiments carried out on a heated R-type (Pt-Rh) thermocouple. The radiation spectrum and the image of the thermocouple bead were obtained simultaneously using a spectrometer and a high-speed camera. Subsequently, the spectral emissivity and temperature of the thermocouple were obtained by using a multi-spectral temperature algorithm, based on the radiation spectrum collected by the spectrometer. As a result, 2D temperature distributions of the R type thermocouple were generated by combining the spectral emissivity measured by the spectrometer and the raw images collected by the high-speed camera. Finally, the temperatures obtained by spectrometer and high-speed camera were compared with, and validated by, the direct temperature measurements of the thermocouple.

2. Principles for measuring temperature and emissivity

The sensor of a high-speed camera receives radiation information from hot objects within its R, G and B response bands, and outputs two-dimensional images from its analog-to-digital converter [12,29,33]. The radiation intensity of the targeted object received by the camera sensor is given by Eq. (1):

$$E_i = \int_{\lambda_1}^{\lambda_2} \varepsilon(\lambda)\cdot\eta_i(\lambda)\cdot I_b\cdot d\lambda\cdot\tau \qquad i = R,\ G,\ B \tag{1}$$

where $\varepsilon(\lambda)$ is the spectral emissivity of the object; $\eta_i(\lambda)$ is the spectral response efficiency function of the camera's i channel (R, G, B), which can be calibrated by using a monochromatic light source [21]; λ_1 and λ_2 are the lower and upper wavelength limits of the spectral response of the high-speed camera, respectively; τ is the shutter time of the high-speed camera; I_b is the blackbody radiation intensity. According to Plank's law, the term I_b can be expressed as:

$$I_b = \frac{C_1\cdot\lambda^{-5}}{e^{C_2/\lambda T_c} - 1} \tag{2}$$

where C_1 and C_2 are Plank constants; T_c is the 2D temperature distribution of the measured object. Substituting Eq. (2) into Eq. (1):

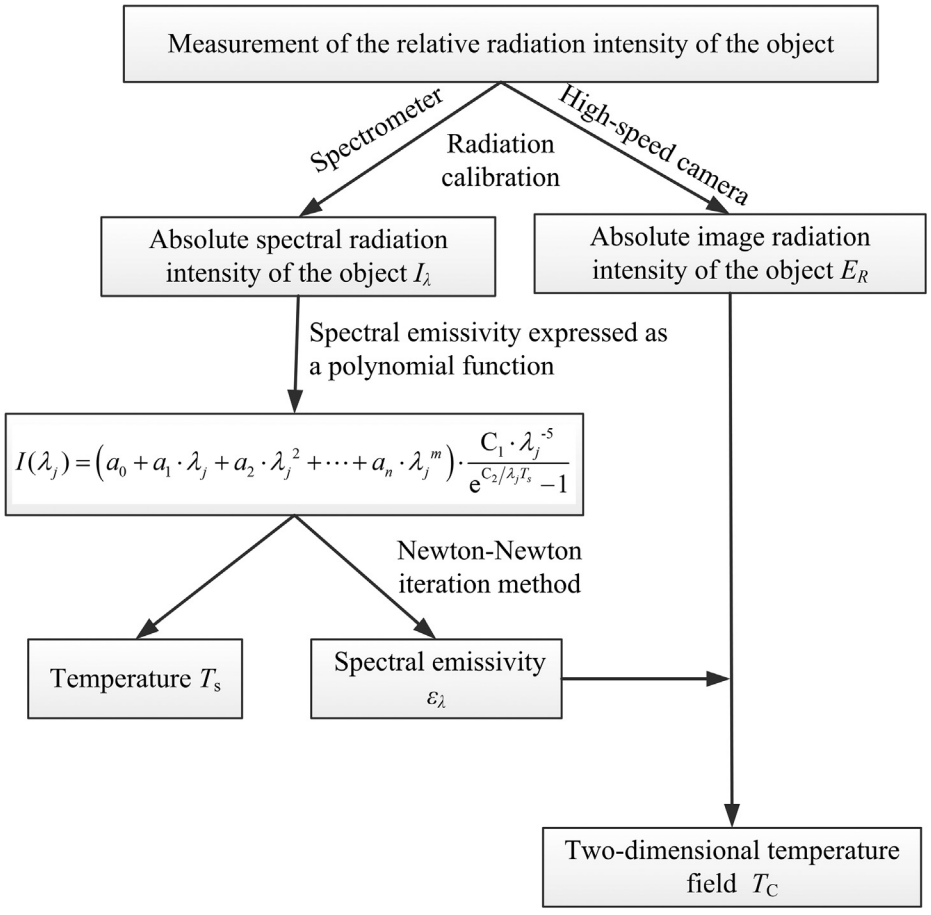

Fig. 1. Flow diagram of the iterative reconstruction algorithm.

$$E_i = \int_{\lambda_1}^{\lambda_2} \varepsilon(\lambda)\cdot\eta_i(\lambda)\cdot\frac{C_1\cdot\lambda^{-5}}{e^{C_2/\lambda T_c}-1}\cdot d\lambda\cdot\tau \quad i = R, G, B \tag{3}$$

The function relation between the radiation intensity E_i and the output image intensity of the high-speed camera, S_i, can be established by calibration using with a known radiation source [12,15]. In this paper, a tungsten ribbon filament lamp was used for radiation calibration. The lamp was pre-calibrated by the US National Institute of Standards and Technology (NIST). Its radiation intensity was regulated by adjusting the input electric current, and it was monitored by the spectrometer. The response wavelength of R channel is larger than that of G which, again, is larger than that of B channel [21,55], as this camera has a visible light sensor. Therefore, the signal-to-noise ratio of the output image of the R channel is the highest under the same shutter speed. As a result, the image output of the R channel of the high-speed camera was adopted in the temperature measurement, so that calibration was only performed on the R channel. The following relation can be established after radiation calibration of the camera using the tungsten lamp:

$$E_R = f(S_R) \tag{4}$$

Considering Eq. (3) and Eq. (4), then:

$$f(S_R) = \int_{\lambda_1}^{\lambda_2} \varepsilon(\lambda)\cdot\eta_i(\lambda)\cdot\frac{C_1\cdot\lambda^{-5}}{e^{C_2/\lambda T_c}-1}\cdot d\lambda\cdot\tau \tag{5}$$

In Eq. (5), there is one known parameter: $f(S_R)$ and two unknown parameters: $\varepsilon(\lambda)$, T_c, hence, it cannot be solved. Therefore, a spectrometer was used to simultaneously monitor the thermocouple bead, and its spectral emissivity $\varepsilon(\lambda)$ was measured in real-time based on spectral analysis. The temperature T_c of the thermocouple was then calculated by substituting the measured emissivity $\varepsilon(\lambda)$ into Eq. (5).

The monochromatic radiation intensity within the range of the response wavelength of the spectrometer can be obtained from the following expression:

$$I(\lambda_j) = \varepsilon(\lambda_j)\cdot\frac{C_1\cdot\lambda_j{}^{-5}}{e^{C_2/\lambda_j T_s}-1} \quad j = 1, 2, 3. \ldots..n \tag{6}$$

where j is the number of measured effective wavelengths within the spectral response range of the spectrometer; T_s is the one-dimensional temperature measured by the spectrometer. The spectral emissivity of a high temperature metal solid surface can be expressed by polynomial function [6,7,37]:

$$\varepsilon(\lambda_j) = a_0 + a_1\cdot\lambda_j + a_2\cdot\lambda_j{}^2 + \cdots + a_n\cdot\lambda_j{}^m \tag{7}$$

where m is the series of polynomial. Substitution of Eq. (7) into Eq. (6), gives:

$$I(\lambda_j) = (a_0 + a_1\cdot\lambda_j + a_2\cdot\lambda_j{}^2 + \cdots + a_n\cdot\lambda_j{}^m)\cdot\frac{C_1\cdot\lambda_j{}^{-5}}{e^{C_2/\lambda_j T_s}-1} \quad j = 1, 2, 3. \ldots..n \tag{8}$$

The spectrometer can measure the radiation intensity in a wide range of wavelengths with very small wavelength intervals. The spectral emissivity of high temperature metal materials may be expressed by a lower order polynomial (the order is usually no more than 4) function [7,37,56,57], hence $m \ll n$. The order m of the polynomial was determined by evaluating the variation of the residual $|f|^2$ at different levels; m was assigned integer values bigger than unity. There is a minimum value of $|f|$ in Eq. (9) which can be obtained numerically by the Newton iteration method:

$$|f|^2 = \sum_{j=1}^{n}\left[I(\lambda_j) - (a_0 + a_1\cdot\lambda_j + a_2\cdot\lambda_j{}^2 + \cdots + a_n\cdot\lambda_j{}^m)\cdot\frac{C_1\cdot\lambda_j{}^{-5}}{e^{C_2/\lambda_j T_s}-1}\right]^2 \quad j = 1, 2, 3\cdots n \tag{9}$$

$a_1, a_2, \cdots a_n$ and T_s can be calculated when $|f|^2$ reaches the minimum value, thereby the spectral emissivity $\varepsilon(\lambda_j)$ and temperature T_s are obtained. Substituting the measured $\varepsilon(\lambda_j)$ into Eq. (5), there remains only one unknown parameter, T_c, and thus the equation can be readily solved. This enables the 2D temperature distribution of the object to be measured. A flow diagram for this algorithm is shown in Fig. 1.

3. Experimental setup and calibration

3.1. Experimental set-up

The schematic diagram of the experimental setup is shown in Fig. 2. A Bunsen burner was modified for the purposes of this experiment to allow mixing fuel and air of measured quantities. For this purpose, the air vents at the sides of the burner were surrounded by a sealed metallic enclosure. Air was introduced to the burner through a hole drilled to the side of the enclosure. The burner nozzle diameter was 50 mm. The flowrates of natural gas and air were metered with calibrated *Matheson* rotameters. Upon ignition of the mixed effluent gases, a premixed flame was obtained. The Pt-Rh thermocouple used in the experiment was of an R type, procured from *Omega Engineering*. The positive lead of the thermocouple contained 13% Rh and 87% Pt. The negative lead of thermocouple was pure Pt. The diameters of the positive and negative filaments of thermocouple were both 0.5 mm. The junction was shaped as a sphere, with a diameter of 1.34 mm. The thermocouple was installed 30 mm above the center of the burner outlet. The thermocouple wires were connected to a data acquisition card by a thermocouple extension cable. The generated voltage signals were processed with the *LabVIEW* program. They were compensated by the cold end (room temperature 25 °C), and then they were converted to temperatures according to an appropriate function relation.

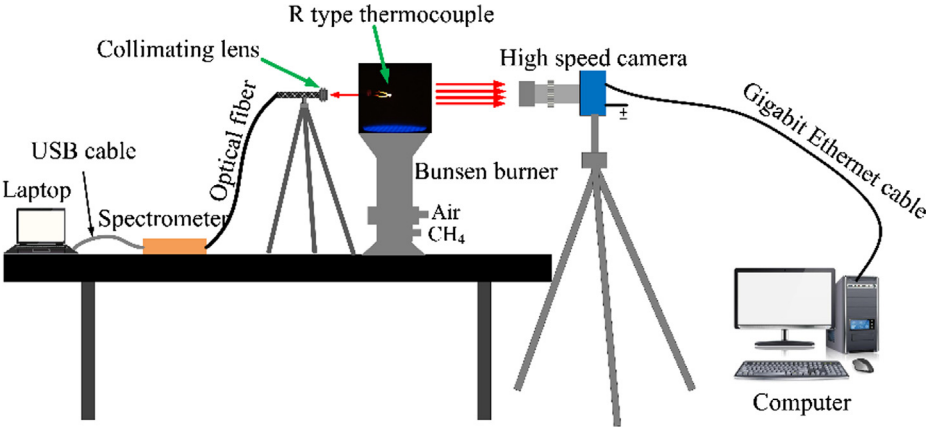

Fig. 2. Schematic of the experimental apparatus.

An *AvaSpec-ULS2048-USB2* spectrometer was used in these experiments to measure radiation intensity. This spectrometer has a Charge Coupled Device (CCD) sensor with a spectral response range from 200 nm to 1100 nm. The spectral resolution is 1.1 nm and the sampling rate is 1.1 ms/scan. The transmission rate is 1.8 ms/scan (USB 2.0). The spectrometer was calibrated using a *Mikron M330* blackbody furnace, derails of which are given in Ref. [15]. The resulting blackbody calibration profiles of the spectrometer at different blackbody furnace temperatures are shown in Fig. 3.

An *Edgertronic SX1* high-speed camera was used in the experiments, fitted with a Complementary Metal Oxide Semiconductor (CMOS) sensor. The camera was coupled to an Olympus-Infinity Model K2 long-distance microscope lens. The maximum frame rate of images acquired by the high-speed camera is 17,791 fps. The relative spectral response efficiency curve of the camera is shown in Fig. 4. The control software of the high-speed camera can output 8-bit uncompressed AVI format video files. Such raw image format (raw data) files contain minimally processed data from the image sensor of the digital camera The MATLAB code was used to read the AVI format video. After reverse *Bayer* decoding, the AVI format video file was converted to TIF format images. The camera was equipped with the aforesaid high-definition lens, which can focus on the thermocouple junction clearly. The high-speed camera has a 16 GB memory card. The collected video files are firstly stored in the memory card, and then they are transferred to the hard disk of a computer through the gigabit ethernet cable.

3.2. Radiation calibrations of the high-speed camera

The functional relationship between the image intensity of the high-speed camera and the radiation intensity of the heated object (in this case the thermocouple bead) is established through radiation calibration using the tungsten lamp. During the calibration experiments, both the high-speed camera and the spectrometer collected images and spectra from both sides of the tungsten lamp. Electric current was supplied to the tungsten lamp in the range of 12.4–15.7 A, with an interval of 0.3 A. The radiation spectral (counts and intensities) of the NIST tungsten filament measured by the spectrometer at different electric current inputs are shown in Fig. 5(a and b). The radiation intensity spectra of tungsten filament are deemed to be smooth between 500 nm and 1000 nm. The radiation intensity increases with the wavelength at any given current, and the radiation intensity increases with increasing current at any given wavelength.

High resolution photographs of the filament of the tungsten lamp collected by the camera, under different electric current settings, are shown in Fig. 6. As the electric current increases, the temperature and, hence, the brightness of the tungsten filament increase gradually. The notch in the filament denotes the location where the NIST calibration was performed.

The functional relationship between the radiative intensity of the lamp's filament and the response of the R channel of the camera is shown in Fig. 7. The relationship between image intensity of the camera and radiation intensity of the lamp when raw data is used ("raw" denotes a not standardized format (unlike TIF, JPG, etc.), and it is a lossless compression format). This is significantly different from the calibration results using non-raw data [13,58]. Thereby, the functional relation depicted in Eq. (4) was established.

4. Experimental results and analysis

Experiments to measure the temperature of the thermocouple remotely were conducted in two different flame conditions, a stable quasi-steady state (stable) flame and an unsteady state (unstable) flame. The latter flames were generated by blowing mild bursts of air sideways to the flame, to momentarily disturb it. In both cases, the flow rate of the natural gas to the Bunsen burner was kept constant, and the flame temperature was adjusted by changing the air flow rate and keeping the fuel flow rate constant. Thus, both the total flowrate of gases and the fuel to air equivalence ratio varied, the latter in the range of 0.82–1.36. The detailed experimental conditions are listed in Table 1.

Flame images, collected by an SLR camera (SONY Alpha 6000) at the four different combustion conditions listed in Table 1, are shown in Fig. 8. All these premixed flames have a translucent light blue color. Their spectral signal intensities were negligible when the flames were observed at the absence of the thermocouple. The amount of soot generated in these flames was very low and the temperature measurement of thermocouple should not be affected by soot accumulation on the junction. The oxygen content of the premixed flames decreased with the decrease of the air flowrate, hence the gradual increase of the equivalent ratio resulted in taller flames, as also observed in Ref. [59].

4.1. Remote measurements of the thermocouple temperature and emissivity in steady flames using the spectrometer method

The spectral radiation intensities of the heated thermocouple, as collected by the spectrometer at four different fuel to air equivalent ratios, are shown in Fig. 9. It can be observed that the radiation intensities of the R-type thermocouple are continuously smooth at wavelengths between 500 nm and 1000 nm, akin to the radiation intensity of the tungsten filament of the NIST lamp, shown in Fig. 5. The strongest spectral radiation intensity of the thermocouple was observed at the equivalence ratio of 0.98, whereas the weakest intensity was observed at the equivalence ratio of 1.36.

Eq. (9) is used for simultaneous calculation of temperature and spectral emissivity based on the measurements of the spectral radiation intensity. During the process of calculation, the series n of the polynomial increases from values starting at $n = 1$. In fact, it was found that Eq. (9) converges when $n = 3$. The calculated spectral emissivity of the thermocouple is shown in Fig. 10. Therein, it can be observed that there is a mild decrease of the spectral emissivity of R type thermocouple with wavelength increasing from 500 nm to 1000 nm. In this band, the decrease in emissivity is more pronounced than that in the band of 800–1000 nm, where the emissivity is nearly-constant. Hence, the thermocouple behaves as a grey body in the latter band. Ma et al. [56] measured the spectral emissivity of the S type thermocouple between 431 nm and 700 nm; the results of that study are also plotted in Fig. 10. The measured spectral emissivities of the R- type thermocouple in this investigation are very close to the values reported by Ma and coworkers for the S-Type thermocouple in the wavelength band of 500–700 nm. For an S-type thermocouple, the Rh content in the positive end of thermocouple is 10% and Pt is 90%. The negative end is also pure Pt. Hence, only the positive end of thermocouple is different

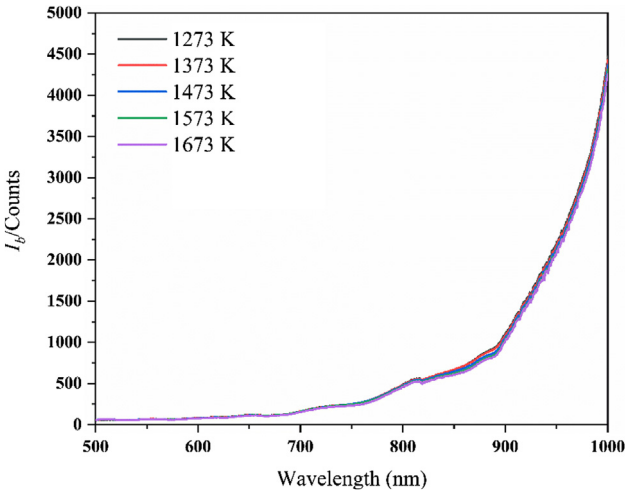

Fig. 3. The blackbody calibration curve of the spectrometer.

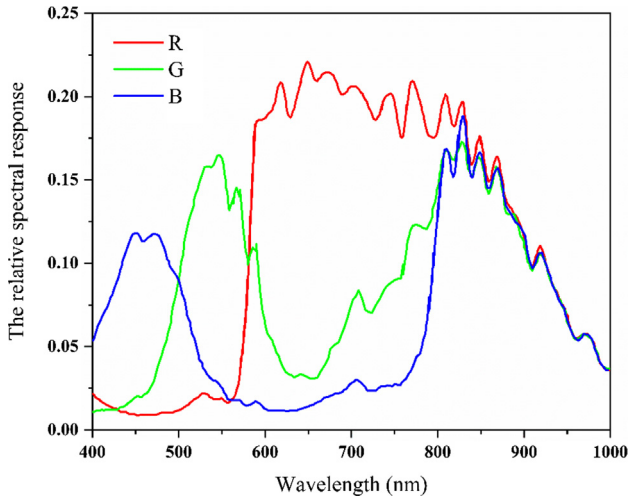

Fig. 4. Relative spectral response curves of the red (R), green (G), and blue (B) wavelenght bands of the *Edgertronic SX1* high-speed camera. (For interpretation of the references to colour in this figure legend, the reader is referred to the web version of this article.)

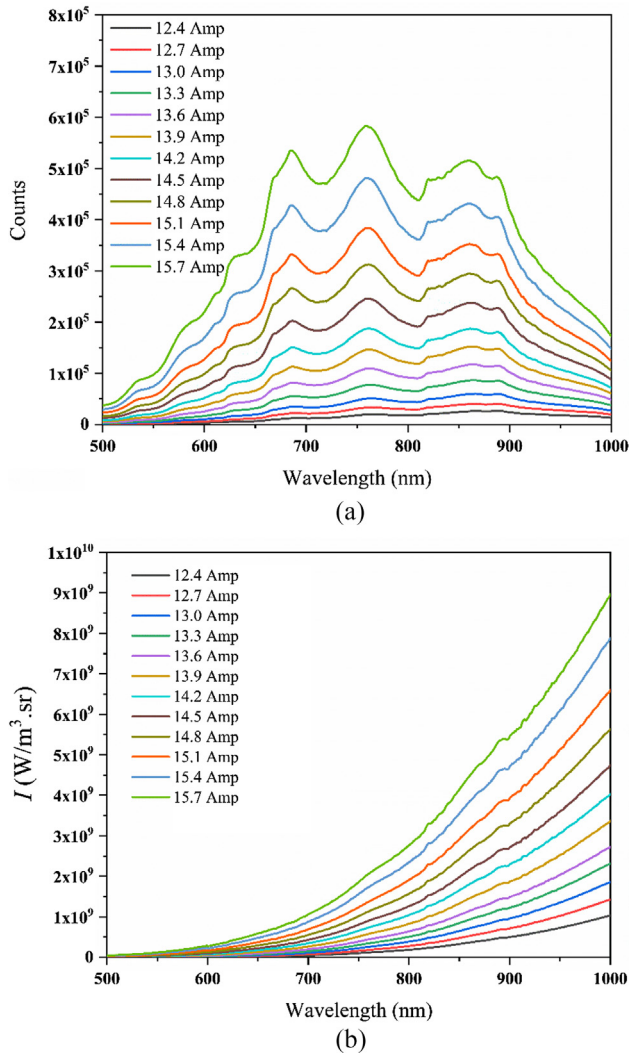

Fig. 5. (a) Counts of the NIST tungsten lamp, and (b) Spectral radiation intensities of the NIST tungsten lamp under different electric current inputs.

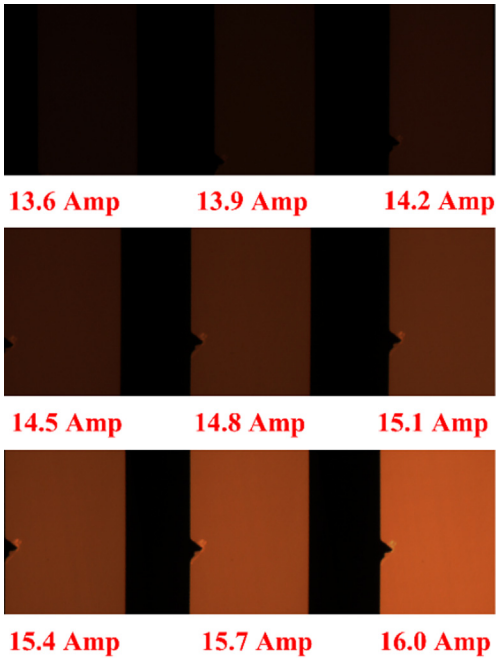

Fig. 6. Images of the filament of the NIST tungsten lamp captured by the high-speed camera under different electric current settings.

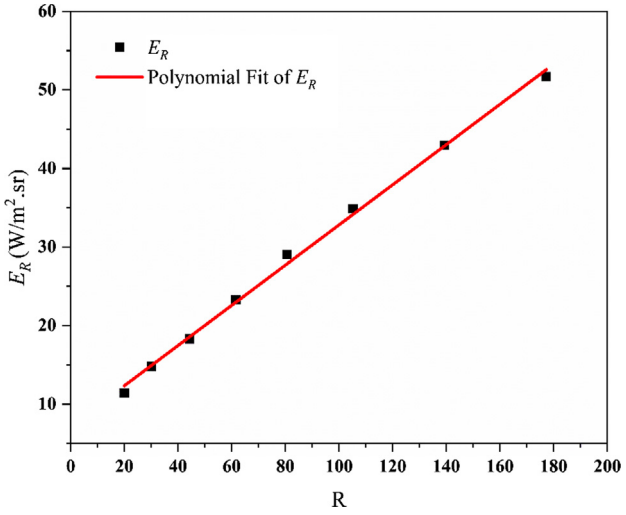

Fig. 7. Calibration of the red (R) response of the digital camera with the radiation intensity, E_R, of the NIST filament lamp. (For interpretation of the references to colour in this figure legend, the reader is referred to the web version of this article.)

Table 1
Summary of the prevailing conditions at four different combustion conditions (flowrates and fuel to air equivalence ratios).

Case	Natural Gas L/min	Air L/min	Total Flowrates L/min	Equivalent Ratio φ
1	0.30	3.50	3.80	0.82
2	0.30	3.30	3.60	0.87
3	0.30	2.90	3.20	0.98
4	0.30	2.10	2.40	1.36

between R type and S type. Ma et al. [56] also showed that the emissivity of pure platinum is very close to that of Pt-Rh containing 90% platinum. The spectrum of pure platinum and of Pt-Rh containing 80% Pt reported by Neuer et al. [60] is also in line with that shown in

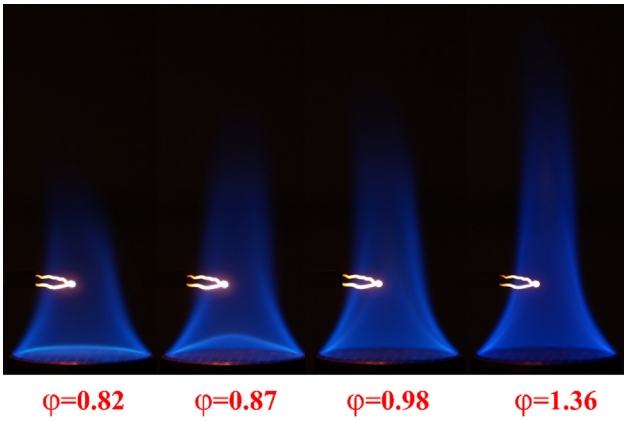

Fig. 8. Images of natural gas flames, with an inserted type-R thermocouple, under the four different combustion conditions listed in Table 1.

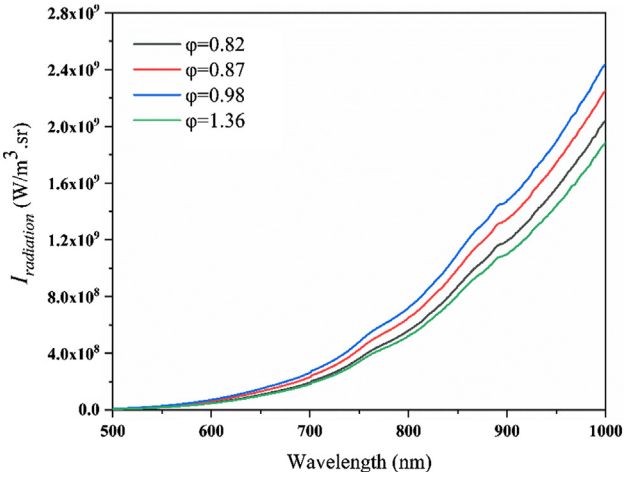

Fig. 9. Spectral radiation intensity of the R-type thermocouple in natural gas/air premixed flames of four different equivalent ratios.

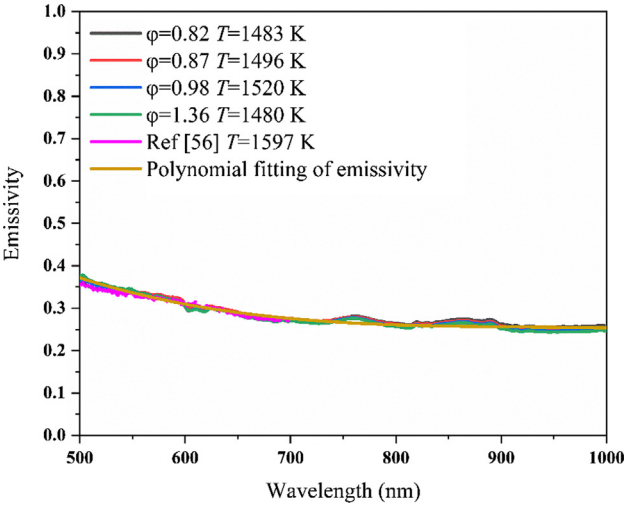

Fig. 10. Spectral emissivity of an R-type thermocouple in the wavelength range of 500–1000 nm.

Fig. 10. Considering all of these results, it can be concluded that the content of Pt in the Pt- Rh alloy has little influence on its spectral emissivity. In the experiments of Ma et al. [56], the temperature range of the thermocouple was 1597–1730 K, and the emissivity of the thermocouple did not change much with temperature in this range.

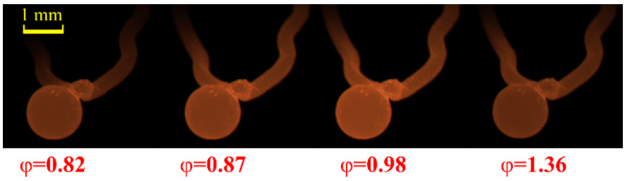

Fig. 11. Raw images of the thermocouple bead and wires heated by premixed flames operated at the four different equivalence ratios of this study.

Worthing et al. [61] measured the spectral emissivity of platinum at temperatures ranging from 1200 K to 1850 K. Their results showed that the emissivity of platinum increased with increasing temperature, but the influence of temperature on the spectral emissivity was found to be modest. The temperature variation range of the four flame conditions herein is 1483 − 1520 K, hence the temperature difference is only 37 K, and the emissivity measured in this temperature range is nearly equal. The spectral emissivity under the four flame conditions can be averaged and the function of emissivity and wavelength can be obtained by polynomial fitting:

$$\varepsilon(\lambda) = 1.4000 - 3.6900 \times 10^{-3} \times \lambda + 3.9878 \times 10^{-6} \times \lambda^2 - 1.4447 \times 10^{-9} \times \lambda^3 ,$$

where λ is in nm.

4.2. Remote measurements of the thermocouple temperature and emissivity in steady flames using the digital camera method

Raw images of the thermocouple bead under the four flame conditions of this study are shown in Fig. 11. It can be observed that the bead image first becomes brighter as flame stoichiometry is approached and reached, and thereafter it becomes dimmer with further increasing the equivalent ratio.

The image intensity recorded by the R channel can be converted into the image of radiation intensity using a function relation between the image intensity and radiation intensity obtained after calibration of the R response of the digital camera with the tungsten filament lamp (Fig. 7). The obtained radiation intensity images are shown in Fig. 12. The radiation intensity of the thermocouple first increased and then decreased with the increase of equivalence ratio, in line with the results of Fig. 11. The radiation intensity was the strongest when the equivalence ratio was 0.98. Moreover, the radiation intensity was not evenly distributed along the filament. The radiation intensity at the spherical bead was relatively uniform. The highest intensity detected at a bulge near the junction. The image displayed in Fig. 12 has a sufficiently high resolution (240 piexls × 220 pixels) to reveal spatial details. Such a high resolution can be considered as an advantage of this method of temperature measurement, which is based on an electronic camera.

The two-dimensional temperature distributions of the thermocouple were calculated by Eq. (5), using the radiation intensity images of the R channel, given in Fig. 12, and substituting the spectral emissivities measured by the spectrometer. Results are shown in Fig. 13. The thermocouple temperature distributions are not spatially uniform. Temperatures at the thermocouple junction are higher than those at the leads. The maximum standard deviation of the thermocouple bead temperature variation in this case was less than 3.3%, throughout three-minute-long sets of data. This temperature fluctuation in the bead was small, hence the flame temperature is rather evenly distributed on the surface of the 1 mm bead. The average temperature of the thermocouple junction denoted by the white square area in Fig. 12 was then calculated to obtain the final temperature measurement by the high-speed camera.

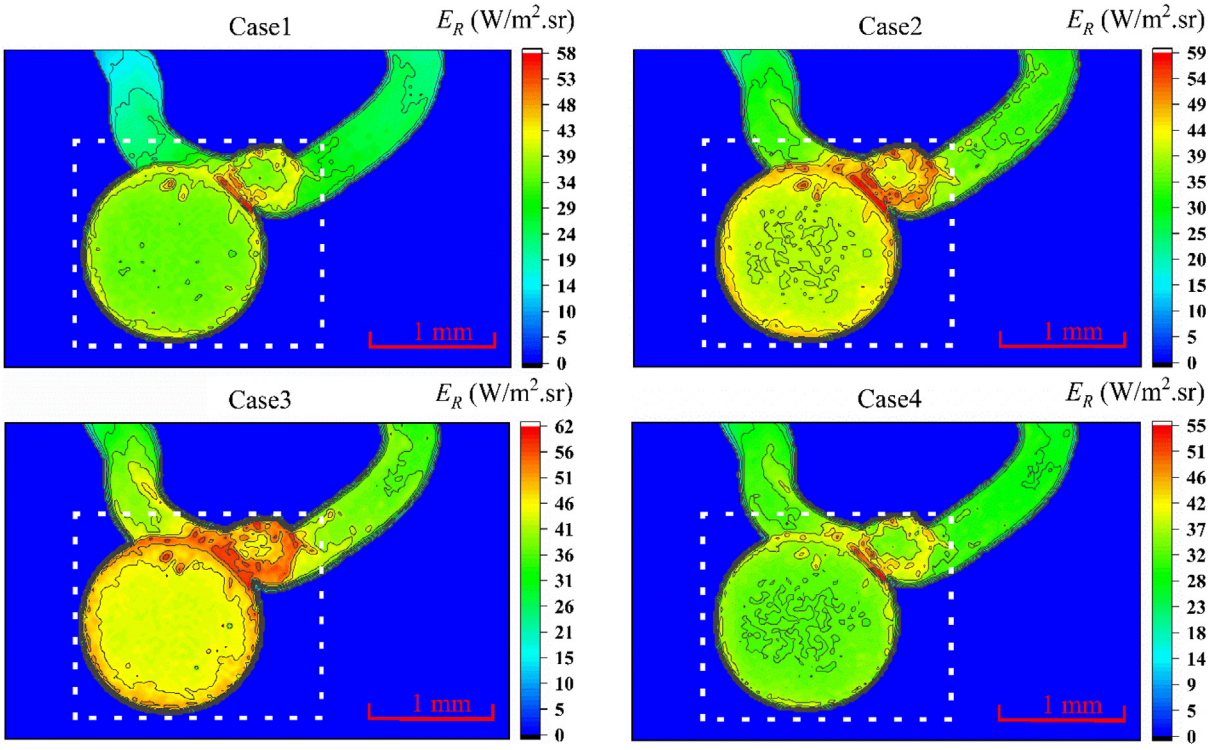

Fig. 12. Radiation intensity images of the thermocouple bead and wires of Fig. 11, obtained from the R channel of the camera.

4.3. Comparison of the thermocouple bead temperature measurements in stable flames by the spectrometer, the digital camera and the thermocouple voltage output

Bead temperature measurements based on the spectrometer and high-speed camera were compared with those obtained from the electromotive force (voltage) output of the thermocouple, and results are shown in Fig. 14. Temperatures varied between 1490 K and 1530 K; they increased first and then decreased with the equivalence ratio of the flame and reached their highest value at φ = 0.98. Compared with the thermocouple measurement results, the maximum absolute error and maximum relative error of the spectrometer measurement results under

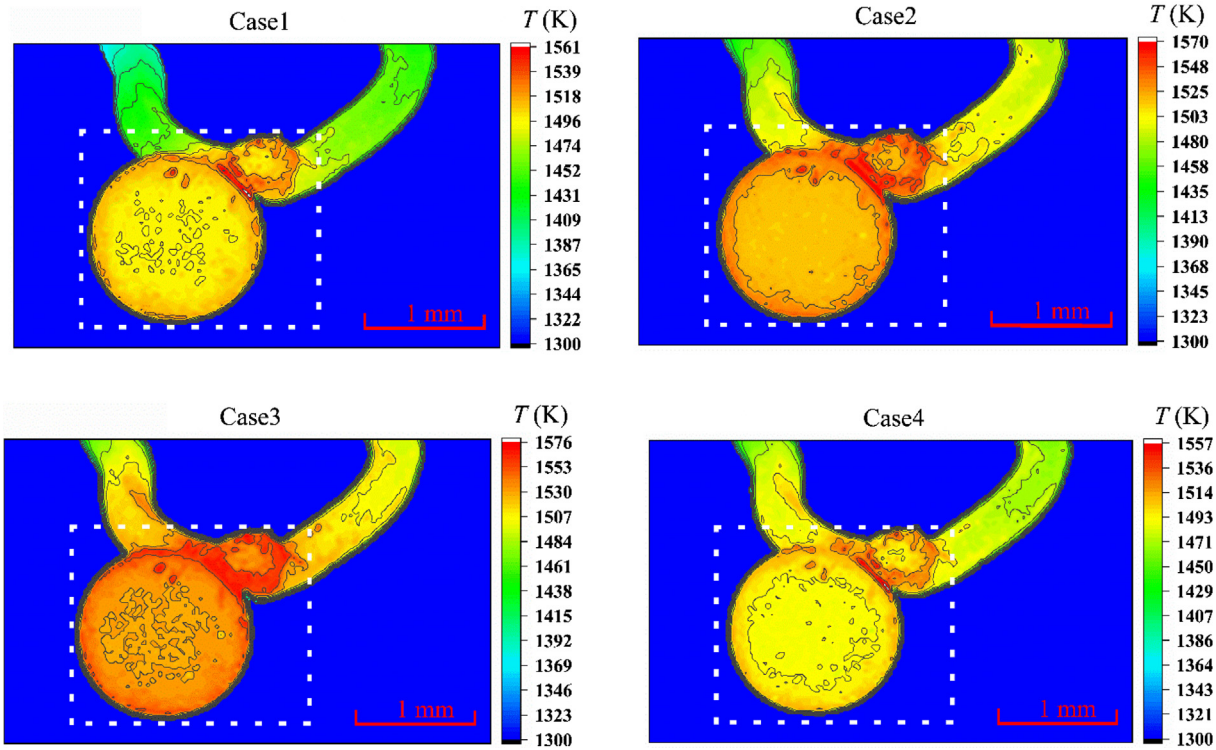

Fig. 13. 2D temperature distributions on the surface of the thermocouple bead and wires obtained from the radiation intensity images of Fig. 12 and spectral emissivity data.

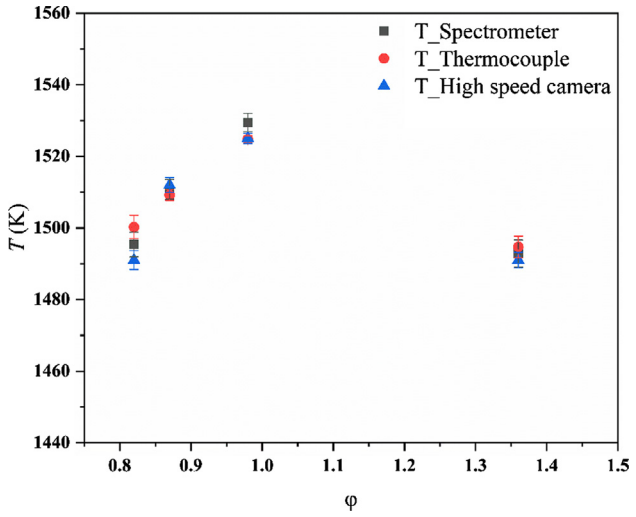

Fig. 14. Comparison of thermocouple bead temperature measured by the spectrometer, the high-speed camera and the thermocouple voltage under four different flame fuel to air equivalence ratios.

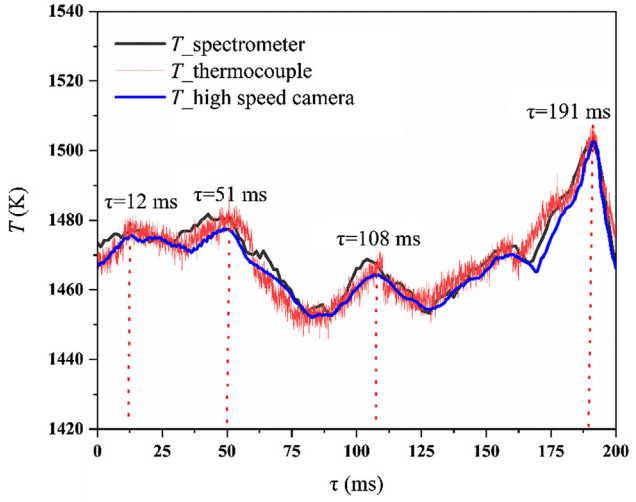

Fig. 15. Comparison of temperatures measured by the thermocouple, the spectrometer and the high-speed camera under unsteady state flame conditions.

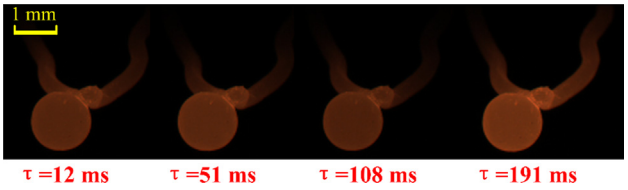

Fig. 16. Raw images of the thermocouple bead at the four different peak temperatures denoted in Fig. 15.

the four different equivalence ratios examined were 4.9 K and 0.32% respectively; The maximum absolute error and the maximum relative error of the temperature measured by the high-speed camera are 9.2 K and 0.62%, respectively, based on 200 sets of continuously collected data. These results show that the temperature measurements of the spectrometer and the high-speed camera have good accuracy.

4.4. Remote measurements of the thermocouple temperature and emissivity in unsteady flames using the digital camera method

In these experiments the flame was disturbed by ambient air flow and burned unsteadily. Photographic images and the radiative spectrum of the thermocouple in such unsteady flame combustion conditions were recorded simultaneously by the high-speed camera and the spectrometer. The sampling frequency of the high-speed acquisition card of the thermocouple in this experimentation was 1.2×10^6 Hz. The sampling frequency of the high-speed camera was 1.8×10^3 Hz. The sampling frequency of the spectrometer was 0.75×10^3 Hz. Fig. 15 shows superimposed time-dependent temperature measurements with the thermocouple, the spectrometer and the high-speed camera, during a sampling period of 200 ms.

The signal output fluctuation of the thermocouple was larger due to the higher sampling frequency of the high-speed acquisition card of thermocouple. The results of temperature measurement by high speed camera, spectrometer and thermocouple were in good agreement. By comparison to the thermocouple, the maximum absolute error and the maximum relative error of the spectrometer temperature measurements in this timeframe were 8 K and 0.55%, respectively. Conversely, the maximum absolute error and the maximum relative error of the high-speed camera temperature measurements were 11 K and 0.75%, respectively.

The four peaks in temperature shown in Fig. 15 correspond to 12 ms, 51 ms, 108 ms and 191 ms, respectively. The thermocouple images recorded by the high-speed camera at those four instances are shown in Fig. 16, and the corresponding calculated two-dimensional temperature distributions are shown in Fig. 17.

5. Conclusions

A method for simultaneous measurement of temperature and spectral emissivity of an R-type thermocouple with spectrometer and high-speed camera has been presented. The results of spectral analysis showed that there is a mild dependence of the emissivity of the R type thermocouple on the wavelength in the band of 500–1000 nm. Hence, the thermocouple bead it is not exactly a graybody in the entirety of this band. However, the emissivity changes little with the wavelength in the narrower band of 800–1000 nm, hence, in this range the thermocouple behaves as a graybody. The spectral emissivity of the R-type thermocouple measured in this paper is consistent with the results of the S-type thermocouple previously measured in the literature in the band of 500–700 nm. This shows that although the content of rhodium in the R-type and S-type thermocouples is different, it does not affect the spectral emissivity of platinum at these wavelengths.

The spectral emissivity of the bead was measured by the spectrometer and, thereafter, it was used to obtain the temperature distribution of the thermocouple based on the readings of the high-speed camera. Thereby, it was demonstrated that this method can also be used to detect two-dimensional temperature field distributions of small particles. Maximum relative errors in thermocouple bead temperatures, obtained under quasi-steady state heating, were 0.32% and 0.62% when obtained by the spectrometer and the camera, respectively, by comparison to the thermocouple output voltage. Maximum relative errors in thermocouple bead temperatures, obtained under unsteady state heating, were 0.55% and 0.75% when obtained by the spectrometer and the camera, respectively, by comparison to the thermocouple output voltage.

These results show that the measurement method described herein has significant measurement accuracy; hence, it is suitable for measuring both steady and transient thermal radiation. In future work, this measurement method will be applied to the combustion of single particles of solid fuels, to obtain their temporal spectral emissivity and temperature changes.

Declaration of Competing Interest

We declare that we have no conflict of interest.

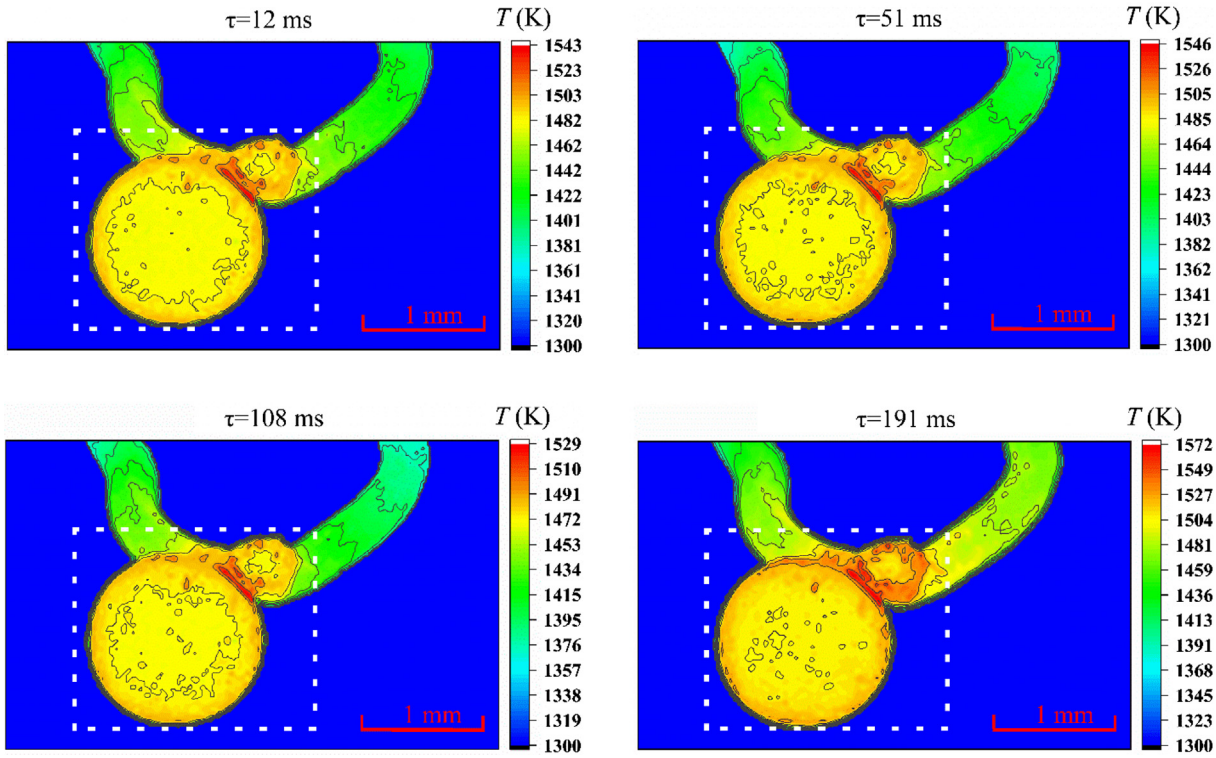

Fig. 17. 2D temperature distributions on the surface of the thermocouple bead and wires of Fig. 16, corresponding to the peak temperatures of Fig. 15.

Acknowledgements

The research was supported by the Natural Science Foundation of China (NO. 51706239), by the China Postdoctoral Science Foundation Grant (NO. 2019M661982) and by the US National Science Foundation Grant # 1810961. W.Y was supported by the China Scholarship Council (NO. 201806425012) during his visit at NU. The authors would like to thank Mr. Michael Matter and Mr. Todd Fisher from Sanstreak Corp. for technical assistance.

References

[1] A. Panahi, S.K. Sirumalla, R.H. West, Y.A. Levendis, Temperature and oxygen partial pressure dependencies of the coal-bound nitrogen to NOx conversion in O_2/CO_2 environments, Combust. Flame. 206 (2019) 98–111.

[2] A. Panahi, N. Vorobiev, M. Schiemann, M. Tarakcioglu, M. Delichatsios, Y.A. Levendis, Combustion details of raw and torrefied biomass fuel particles with individually-observed size, shape and mass, Combust. Flame. 207 (2019) 327–341.

[3] T. Konishi, A. Ito, Y. Kudo, A. Narumi, K. Saito, J. Baker, P.M. Struk, Simultaneous measurement of temperature and chemicalspecies concentrations with a holographic interferometer and infrared absorption, Appl. Opt. 45 (22) (2006) 5725–5732.

[4] Z.J. Diao, M. Winter, T. Hirasawa, K. Saito, Characterization of the thermal structure of six clustered microflames seeded with TaN particles through emission spectroscopy, Exp. Therm. Fluid. Sci. 96 (2018) 295–302.

[5] Z.J. Diao, M. Winter, T. Hirasawa, Y. Kato, Y. Ishino, K. Saito, Characterization of six clustered methane-air diffusion microflames through spectroscopic and tomographic analysis of CH* and C2* chemiluminescence, Exp. Therm. Fluid. Sci. 102 (2019) 20–27.

[6] C.D. Wen, Y.H. Chr, The assessment of multispectral radiation thermometry using linear and log-linear emissivity models for steel, Numer. Heat Tranf. B. 58 (1) (2010) 40–54.

[7] C.D. Wen, T.Y. Chai, Experimental investigation of emissivity of aluminum alloys and application of multispectral radiation thermometry, Appl. Therm. Eng. 31 (14–15) (2011) 2414–2421.

[8] P. Hagqvist, F. Sikstrom, A.K. Christiansson, B. Lennartson, Emissivity compensated spectral pyrometry for varying emissivity metallic measurands, Meas. Sci. Technol. 25 (2014) 025010.

[9] P. Wang, Z.W. Hu, Z. Xie, M. Yan, A new experimental apparatus for emissivity measurements of steel and the application of multi-wavelength thermometry to continuous casting billets, Rev. Scient. Instrum. 89 (5) (2018) 054903, https://doi.org/10.1063/1.5007225.

[10] M.M. Hossain, G. Lu, Y. Yan, Measurement of Flame Temperature distribution using optical tomographic and two-color pyrometric techniques, in: 2012 IEEE International Instrumentation and Measurement Technology Conference, IEEE: New York, 2012, pp. 1856–1860.

[11] M.M. Hossain, G. Lu, D. Sun, Y. Yan, Three-dimensional reconstruction of flame temperature and emissivity distribution using optical tomographic and two-colour pyrometric techniques, Meas. Sci. Technol. 24 (2013) 7.

[12] W.J. Yan, C. Lou, Two-dimensional distributions of temperature and soot volume fraction inversed from visible flame images, Exp. Therm. Fluid. Sci. 50 (2013) 229–233.

[13] C. Lou, X.B. Chen, W.J. Yan, Y.F. Tian, B.M. Kumfer, Effect of stoichiometric mixture fraction on soot fraction and emission spectra with application to oxy-combustion, Proc. Combust. Inst. 37 (4) (2019) 4571–4578.

[14] Y. Xu, S.Q. Li, Y. Yuan, Q. Yao, Measurement on the surface temperature of dispersed chars in a flat-flame burner using modified RGB pyrometry, Energ. Fuel. 31 (3) (2017) 2228–2235.

[15] W.J. Yan, H.C. Zhou, Z.W. Jiang, C. Lou, X.K. Zhang, D.L. Chen, Experiments on measurement of temperature and emissivity of municipal solid waste (MSW) combustion by spectral analysis and image processing in visible spectrum, Energ. Fuel. 27 (11) (2013) 6754–6762.

[16] X.Y. Zhang, X. Lu, Y. Yang, B. Zhang, H.J. Xu, Temperature measurement of coal fired flame in the cement kiln by raw image processing, Measurement 129 (2018) 471–478.

[17] J. Hees, D. Zabrodiec, A. Massmeyer, O. Hatzfeld, R. Kneer, Experimental investigation into the influence of the oxygen concentration on a pulverized coal swirl flame in oxy-fuel atmosphere, Fuel 240 (2019) 64–74.

[18] L.C. Shao, Z.J. Zhou, L.P. Chen, L.Z. Guo, B.J. Chen, L.J. Liang, Study of an improved two-colour method integrated with the emissivity ratio model and its application to air- and oxy-fuel flames in industrial furnaces, Measurement 123 (2018) 54–61.

[19] H.J. Wang, Z.F. Huang, D.D. Wang, Z.X. Luo, Y.P. Sun, Q.Y. Fang, C. Lou, H.C. Zhou, Measurements on flame temperature and its 3D distribution in a 660 MWe arch-fired coal combustion furnace by visible image processing and verification by using an infrared pyrometer, Meas. Sci. Technol. 20 (11) (2009).

[20] C. Lou, H.C. Zhou, P.F. Yu, Z.W. Jiang, Measurements of the flame emissivity and radiative properties of particulate medium in pulverized-coal-fired boiler furnaces by image processing of visible radiation, Proc. Combust. Inst. 31 (2) (2007) 2771–2778.

[21] W.J. Yan, S. Zheng, H.C. Zhou, Experiments investigation on 2D distribution of soot temperature and volume fraction by image processing of visible radiation, Appl. Therm. Eng. 124 (2017) 1014–1022.

[22] T.J. Li, J. Sun, Y. Yuan, C.L. Xu, Y. Shuai, H.P. Tan, Simulation of calibration process in flame measurement by plenoptic camera, Appl. Therm. Eng. 135 (2018) 179–187.

[23] J.A.H. Dreyer, R.I. Slavchov, E.J. Rees, J. Akroyd, M. Salamanca, S. Mosbach, M. Kraft, Improved methodology for performing the inverse Abel transform of flame images for color ratio pyrometry, Appl. Opt. 58 (10) (2019) 2662–2670.

[24] M.J. Ni, H.D. Zhang, F. Wang, Z.C. Xie, Q.X. Huang, J.H. Yan, K.F. Cen, Study on the

detection of three-dimensional soot temperature and volume fraction fields of a laminar flame by multispectral imaging system, Appl. Therm. Eng. 96 (2016) 421–431.
[25] X. Huang, H. Qi, X.L. Zhang, Y.T. Ren, L.M. Ruan, H.P. Tan, Application of land-weber method for three-dimensional temperature field reconstruction based on the light-field imaging technique, J. Heat Transf.-Trans. ASME., 140 (8) 2018.
[26] L. Shen, D.M. Zhu, S. Nadeem, Z.Q. Wang, A.E. Kaufman, Radiative transport based flame volume reconstruction from videos, IEEE Trans. Vis. Comput. Graph. 24 (7) (2018) 2209–2222.
[27] J. Smart, G. Lu, Y. Yan, G. Riley, Characterisation of an oxy-coal flame through digital imaging, Combust. Flame 157 (6) (2010) 1132–1139.
[28] H.C. Hottel, F.P. Broughton, Determination of true temperature and total radiation from luminous gas flames, Industr. Eng. Chem. Anal. Ed. 4 (1932) 166–175.
[29] P.B. Kuhn, B. Ma, B.C. Connelly, M.D. Smooke, M.B. Long, Soot and thin-filament pyrometry using a color digital camera, Proc. Combust. Inst. 33 (2011) 743–750.
[30] J.D. Maun, P.B. Sunderland, D.L. Urban, Thin-filament pyrometry with a digital still camera, Appl. Opt. 46 (4) (2007) 483–488.
[31] M. Vicariotto, D. Dunn-Rankin, Temperature profiles and extinction limits of a coflow water-vapor laden methane/air diffusion flame, Exp Fluids 59 (9) (2018), https://doi.org/10.1007/s00348-018-2589-x.
[32] D. Sun, G. Lu, H. Zhou, Y. Yan, Measurement of soot temperature, emissivity and concentration of a Heavy-Oil flame through pyrometric imaging, in: IEEE International Instrumentation and Measurement Technology Conference, IEEE: New York, 2012, pp. 1865–1869.
[33] T.S. Draper, D. Zeltner, D.R. Tree, Y. Xue, R. Tsiava, Two-dimensional flame temperature and emissivity measurements of pulverized oxy-coal flames, Appl. Energ. 95 (2012) 38–44.
[34] R. Khatami, Y.A. Levendis, On the deduction of single coal particle combustion temperature from three-color optical pyrometry, Combust. Flame 158 (9) (2011) 1822–1836.
[35] Y.A. Levendis, K.R. Estrada, H.C. Hottel, Development of multicolor pyrometers to monitor the transient response of burning carbonaceous particles, Rev. Sci. Instrum. 63 (1992) 3608–3622.
[36] S. Deep, Y. Krishna, G. Jagadeesh, Temperature characterization of a radiating gas layer using digital-single-lens-reflex-camera-based two-color ratio pyrometry, Appl. Opt. 56 (30) (2017) 8492–8500.
[37] A. Araujo, Multi-spectral pyrometry-a review, Meas. Sci. Technol. 28 (8) (2017).
[38] M.A. Khan, C. Allemand, T.W. Eagar, Noncontact temperature-measurement. 2. Least-squares based techniques, Rev. Sci. Instrum. 62 (2) (1991) 403–409.
[39] J. Xing, S.L. Cui, W.G. Qi, F.C. Zhang, X.G. Sun, W.M. Sun, A data processing algorithm for multi-wavelength pyrometry-which does not need to assume the emissivity model in advance, Measurement 67 (2015) 92–98.
[40] Y.P. Sun, C. Lou, H.C. Zhou, A simple judgment method of gray property of flames based on spectral analysis and the two-color method for measurements of temperatures and emissivity, Proc. Combust. Inst. 33 (2011) 735–741.
[41] T. Parameswaran, R. Hughes, P. Gogolek, P. Hughes, Gasification temperature measurement with flame emission spectroscopy, Fuel 134 (2014) 579–587.
[42] T. Parameswaran, M.A. Duchesne, S. Champagne, R.W. Hughes, Petroleum coke gasification temperatures and flame spectra in the visible region at high pressure, Energ. Fuel 30 (11) (2016) 9867–9875.
[43] H.W. Liu, S. Zheng, H.C. Zhou, C.B. Qi, Measurement of distributions of temperature and wavelength-dependent emissivity of a laminar diffusion flame using hyper-spectral imaging technique, Meas. Sci. Technol. 27 (2) (2016) 025201, https://doi.org/10.1088/0957-0233/27/2/025201.
[44] W. Devesse, D. De Baere, P. Guillaume, High resolution temperature measurement of liquid stainless steel using hyperspectral imaging, Sensors 17 (1) (2017).
[45] T.R. Fu, J.F. Liu, M.H. Duan, S. Li, Subpixel temperature measurements in plasma jet environments using high-speed multispectral pyrometry, J. Heat Transf.-Trans. ASME, 140 (7) (2018).
[46] M.T. Si, Q. Cheng, Q. Zhang, D. Wang, Z.X. Luo, C. Lou, Study of temperature, apparent spectral emissivity, and soot loading of a single burning coal particle using hyper-spectral imaging technique, Combust. Flame 209 (2019) 267–277.
[47] J.M. Densmore, M.M. Biss, K.L. McNesby, B.E. Homan, High-speed digital color imaging pyrometry, Appl. Opt. 50 (17) (2011) 2659–2665.
[48] M. Jakob, P. Lehnen, P. Adomeit, S. Pischinger, Development and application of a stereoscopic 3-color high-speed ratio-pyrometry, Combust. Flame 161 (11) (2014) 2825–2841.
[49] B. Bizjan, B. Širok, J. Drnovšek, I. Pušnik, Temperature measurement of mineral melt by means of a high-speed camera, Appl. Opt. 54 (26) (2015) 7978–7984.
[50] K.L. McNesby, B.E. Homan, R.A. Benjamin, V.M. Boyle, J.M. Densmore, M.M. Biss, Invited Article: quantitative imaging of explosions with high-speed cameras, Rev. Scient. Instrum. 87 (5) (2016) 051301, https://doi.org/10.1063/1.4949520.
[51] B. Lou, Y. Wang, X.F. Long, F. Tian, Area Rules for the diffusion flame of a moving Bunsen burner corresponding to different temperature ranges, Combust. Explos. 53 (5) (2017) 517–525.
[52] L.C. Yao, C.Y. Wu, Y.C. Wu, L.H. Chen, J. Chen, X.C. Wu, K.F. Cen, Investigating particle and volatile evolution during pulverized coal combustion using high-speed digital in-line holography, Proc. Combust. Inst. 37 (3) (2019) 2911–2918.
[53] R. Khatami, Y.A. Levendis, An overview of coal rank influence on ignition and combustion phenomena at the particle level, Combust. Flame 164 (2016) 22–34.
[54] J. Riaza, R. Khatami, Y.A. Levendis, L. Alvarez, M.V. Gil, C. Pevida, F. Rubiera, J.J. Pis, Single particle ignition and combustion of anthracite, semi-anthracite and bituminous coals in air and simulated oxy-fuel conditions, Combust. Flame. 161 (4) (2014) 1096–1108.
[55] T. Fu, Z. Yang, L. Wang, X. Cheng, M. Zhong, C. Shi, Measurement performance of an optical CCD-based pyrometer system, Opt. Laser. Technol. 42 (4) (2010) 586–593.
[56] B. Ma, M.B. Long, Absolute light calibration using S-type thermocouples, Proc. Combust. Inst. 34 (2) (2013) 3531–3539.
[57] J.C. De Vos, A new determination of the emissivity of tungsten ribbon, Physica 20 (7) (1954) 690–714.
[58] W. Li, C. Lou, Y. Sun, H. Zhou, Estimation of radiative properties and temperature distributions in coal-fired boiler furnaces by a portable image processing system, Exp. Therm. Fluid. Sci. 35 (2) (2011) 416–421.
[59] A. Michalakou, G. Skevis, S. Couris, P. Stavropoulos, Quantitative local equivalence ratio determination in laminar premixed methane–air flames by laser induced breakdown spectroscopy (LIBS), Chem. Phys. Lett. 404 (2005) 309–314.
[60] G. Neuer, G. Jaroma-Weiland, Spectral and total emissivity of high-temperature materials, Int. J. Thermophys. 19 (3) (1998) 917–929.
[61] A.G. Worthing, Spectral emissivities of tantalum, platinum, nickel and gold as a function of temperature, and the melting point of tantalum, Phys. Rev. 28 (1) (1926) 174–189.